Laurentide ice-sheet instability during the last deglaciation

Citation	Ullman, D. J., Carlson, A. E., Anslow, F. S., LeGrande, A. N., & Licciardi, J. M. (2015). Laurentide ice-sheet instability during the last deglaciation. Nature Geoscience, 8(7), 534-540. doi:10.1038/NGEO2463
DOI	10.1038/NGEO2463
Publisher	Nature Publishing Group
Version	Version of Record
Terms of Use	http://cdss.library.oregonstate.edu/sa-termsofuse

LETTERS
PUBLISHED ONLINE: 22 JUNE 2015 | DOI: 10.1038/NGEO2463

nature geoscience

Laurentide ice-sheet instability during the last deglaciation

David J. Ullman[1,2]*, Anders E. Carlson[1,2]*, Faron S. Anslow[3], Allegra N. LeGrande[4] and Joseph M. Licciardi[5]

Changes in the amount of summer incoming solar radiation (insolation) reaching the Northern Hemisphere are the underlying pacemaker of glacial cycles[1–6]. However, not all rises in boreal summer insolation over the past 800,000 years resulted in deglaciation to present-day ice volumes[1–3,6–8], suggesting that there may be a climatic threshold for the disappearance of land-based ice. Here we assess the surface mass balance stability[9] of the Laurentide ice sheet—the largest glacial ice mass in the Northern Hemisphere—during the last deglaciation (24,000 to 9,000 years ago). We run a surface energy balance model[10,11] with climate data from simulations with a fully coupled atmosphere–ocean general circulation model for key time slices during the last deglaciation. We find that the surface mass balance of the Laurentide ice sheet was positive throughout much of the deglaciation, and suggest that dynamic discharge was mainly responsible for mass loss during this time. Total surface mass balance became negative only in the early Holocene, indicating the transition to a new state where ice loss occurred primarily by surface ablation. We conclude that the Laurentide ice sheet remained a viable ice sheet before the Holocene and began to fully deglaciate only once summer temperatures and radiative forcing over the ice sheet increased by 6–7 °C and 16–20 W m^{-2}, respectively, relative to full glacial conditions.

Evidence for rapid mass loss in past ice sheets[4,12] suggests that ice-sheet instability may be a characteristic of ice-volume hysteresis due to warming climate and associated internal feedbacks[6,8,13–15]. Once a forcing threshold is crossed, an ice sheet will transition to another stable state[9,15,16]. In the case of the Greenland ice sheet, this threshold is defined as the transition from positive to negative surface mass balance (its present surface mass balance is positive and counterbalanced by dynamic mass loss through calving)[9,17]. For large Quaternary glaciations, such an instability should be a climatic threshold for land-based ice sheets to ultimately disappear through a negative surface mass balance[9], potentially preconditioned by ice-sheet geometry[6,11,18]. The gradual deglacial rise in boreal summer insolation and atmospheric CO_2 concentration[5,19,20] provide an opportunity to analyse whether Northern Hemisphere ice sheets exhibited threshold behaviour leading to inexorable deglaciation[3,4,6,15,18,21,22]. If such a threshold existed, this could explain why some intervals of rising boreal summer insolation culminated in near-complete deglaciation of the Laurentide ice sheet (LIS), whereas other insolation rises were followed by only partial deglaciation, with ice sheets persisting over Canada[2,3,6,7].

We examine LIS surface mass balance stability across the last deglaciation to test for the existence of a deglacial threshold. We focus on the LIS because it was the largest of the Northern Hemisphere ice sheets and also the last to disappear[4,12], meaning it was the controlling factor on when the Earth entered the current interglacial period. Deglacial climate was simulated with the NASA Goddard Institute for Space Studies atmosphere–ocean general circulation model (AOGCM) ModelE2-R at specific time periods (24, 21, 19, 16.5, 15.5, 14, 13, 11.5, and 9 thousand years ago (kyr BP)). This climate was used to force a surface energy balance model (SEBM; refs 10,11) of the LIS with climate output from the AOGCM at these specific time slices when the LIS extent is well mapped[12,23] (Fig. 1f,g) and its surface topography has been reconstructed based on the underlying substrate[24] (Supplementary Fig. 1). The LIS reconstructions used in our SEBM are consistent with the AOGCM topography and provide a realistic representation of the low-angle southern LIS margin profile[24] (see Methods).

Our study makes two crucial distinctions from previous simulations of deglacial LIS mass change[6,8,18,25]. First, we use a SEBM because it incorporates a number of variables that affect surface melt beyond just temperature (for example, net longwave/shortwave radiation, sensible/latent heat flux, energy from melting/refreezing)[10,11]. With a few exceptions[15,26], previous simulations have used positive degree-day (PDD) methods that parameterize surface melt as a function of only surface air temperature[6,8,18]. PDD parameters are empirically derived from modern conditions and do not explicitly consider the direct impact of deglacial changes in insolation on surface mass balance[27].

Second, we exclude transient ice dynamics in favour of using known LIS extents with static topographic reconstructions based on flow-line simulations. Although previous dynamic simulations may capture the general size and shape of the LIS (refs 6,8, 15,18,21,22), they do not resolve the topography and individual lobes of the LIS southern margin, and also do not match known intervals of deglacial LIS extent[12,23,24]. For both PDD and SEBM assessments of surface mass balance, such low-angle geometry that matches known LIS extents is necessary for representing the true size of the LIS ablation zone and documenting potential stability thresholds.

Therefore, it is not possible with these previous PDD-dynamic approaches to relate known deglacial LIS extents to radiative forcings to test if the LIS at a given time had a stable or a negative surface mass balance. Here, we use a known LIS extent and concurrent climate forcing to assess if the LIS would inevitably

[1]Department of Geoscience, University of Wisconsin-Madison, Madison, Wisconsin 53706, USA. [2]College of Earth, Ocean, and Atmospheric Sciences, Oregon State University, Corvallis, Oregon 97331, USA. [3]Pacific Climate Impacts Consortium, University of Victoria, Victoria, British Columbia V8W 2Y2, Canada. [4]NASA Goddard Institute for Space Studies & Center for Climate System Research, Columbia University, New York, New York 10025, USA. [5]Department of Earth Sciences, University of New Hampshire, Durham, New Hampshire 03824, USA. *e-mail: dullman@coas.oregonstate.edu; acarlson@coas.oregonstate.edu

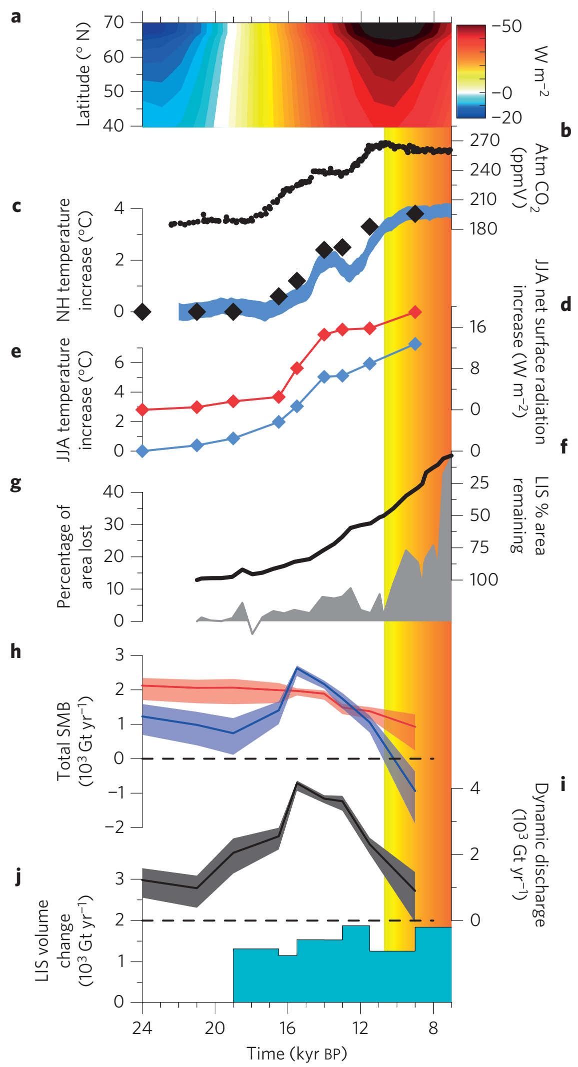

Figure 1 | Deglacial forcings of surface mass balance and model results. **a**, Map of boreal summer insolation anomalies (colour shading) relative to present[19]. **b**, Atmospheric CO_2 concentration[20]. **c**, Northern Hemisphere stack of surface temperature change from 21 kyr BP (blue shaded bar)[5]. Black diamonds show corresponding AOGCM temperature anomalies from 24 kyr BP. **d**, AOGCM summer (June, July, August) net surface radiation increase (from 24 kyr BP) over the LIS (red diamonds). **e**, AOGCM summer (JJA) surface air temperature increase (from 24 kyr BP) over the LIS (blue diamonds). **f**, Percentage area of LIS remaining[23]. **g**, Percentage of LIS area lost relative to previous time slice (shaded grey region)[23]. **h**, Comparison of surface mass balance (SMB) over the entire LIS from the SEBM (blue) and PDD (red). Solid line is the median value, with shaded regions indicating the upper (95%) and lower (5%) quantiles of the simulations. **i**, Estimated rate of dynamical discharge (grey shading indicates uncertainty as propagated from surface mass balance results). **j**, Rate of LIS volume change[24] (light blue). The vertical shaded bar indicates earliest possible timing of the transition to negative total SMB.

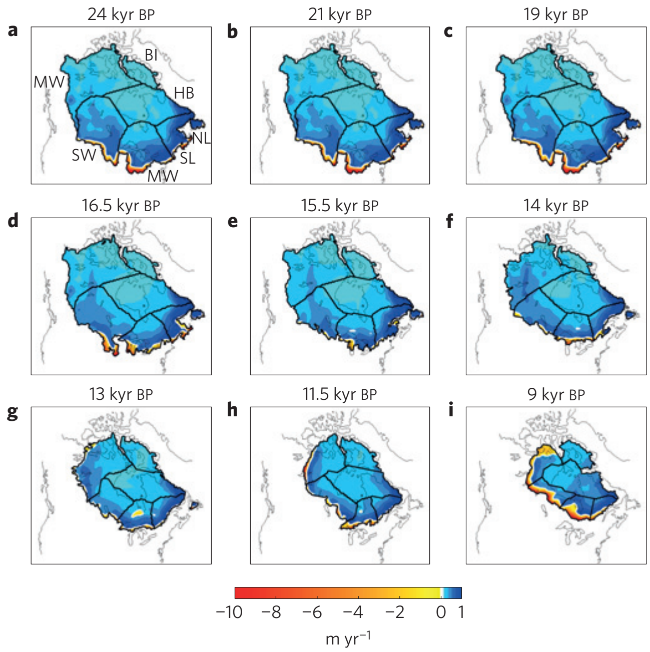

Figure 2 | Simulated surface mass balance maps for the LIS. Maps at 24 kyr BP (**a**), 21 kyr BP (**b**), 19 kyr BP (**c**), 16.5 kyr BP (**d**), 15.5 kyr BP (**e**), 14 kyr BP (**f**), 13 kyr BP (**g**), 11.5 kyr BP (**h**) and 9 kyr BP (**i**). Location of the equilibrium line is marked by solid white line, and boundaries between the ice-sheet sectors are drawn with black lines. The abbreviations of the sectors are St Lawrence (SL), Midwestern (MW), Southwestern (SW), Northwestern (NW), Hudson Bay (HB), Baffin Island (BI) and Newfoundland (NL).

deglaciate at a given time period owing to negative surface mass balance. Such a negative surface mass balance provides a upper limit on the forcing threshold for deglaciation[15,16]. By evaluating LIS surface mass balance and volume change, we can also infer the component of mass change due to dynamic discharge.

Our deglacial ModelE2-R simulations compare well with reconstructions of deglacial Northern Hemisphere temperature[5] (Fig. 1c), suggesting that our time-slice approach captures much of the deglacial hemispheric temperature change. ModelE2-R contains water isotope tracers that agree with past $\delta^{18}O$ records, suggesting that the AOGCM also captures general changes in the hydrologic cycle (Supplementary Fig. 2 and see Methods). At 24 and 21 kyr BP, our surface mass balance results are consistent with the range of previous SEBM results for the last glacial maximum[26]. Despite a gradual increase in radiative forcing (Fig. 1a,b) and attendant warming over the LIS from 24 to 9 kyr BP (Fig. 1d,e), the simulated LIS surface mass balance remains positive from 24 to 11.5 kyr BP, with an increase to peak surface mass balance at 15.5 kyr BP (Figs 1h and 2). After 15.5 kyr BP, surface mass balance declines, reaching negative values by 9 kyr BP (Figs 1h and 2). This transition to negative surface mass balance by 9 kyr BP occurs after only a small additional increase in surface radiative forcing and temperature from 11.5 kyr BP relative to the full deglacial forcing change. Although bias in the AOGCM forcings is probably minimal (Fig. 1c), a slight shift in the timing of this transition is possible, but would still have probably occurred between 11.5 and 9 kyr BP (see Methods).

Using the surface temperature from ModelE2-R over the same LIS topography, we estimate surface ablation using a PDD scheme with a range of scaling and refreezing factors from previous LIS simulations[6,8,18,25] (Fig. 2h and see Methods). The deglacial trend in PDD surface mass balance exhibits a more linear decrease across the deglaciation, without the positive mass balance peak at 15.5 kyr BP. The PDD surface mass balance never becomes negative (except under extreme PDD scaling factors; see Methods), implying the need for substantial dynamic discharge throughout the entire deglaciation to account for deglacial changes in ice volume. Even when the LIS is mainly land-based[23], the PDD scheme simulates that the LIS would never deglaciate through surface ablation, in conflict with observations[28]. These large differences in deglacial surface mass balance trend suggest that the direct influence of the evolving shortwave and longwave radiation[24] is an important forcing, which was not included in previous PDD simulations[6,8,18].

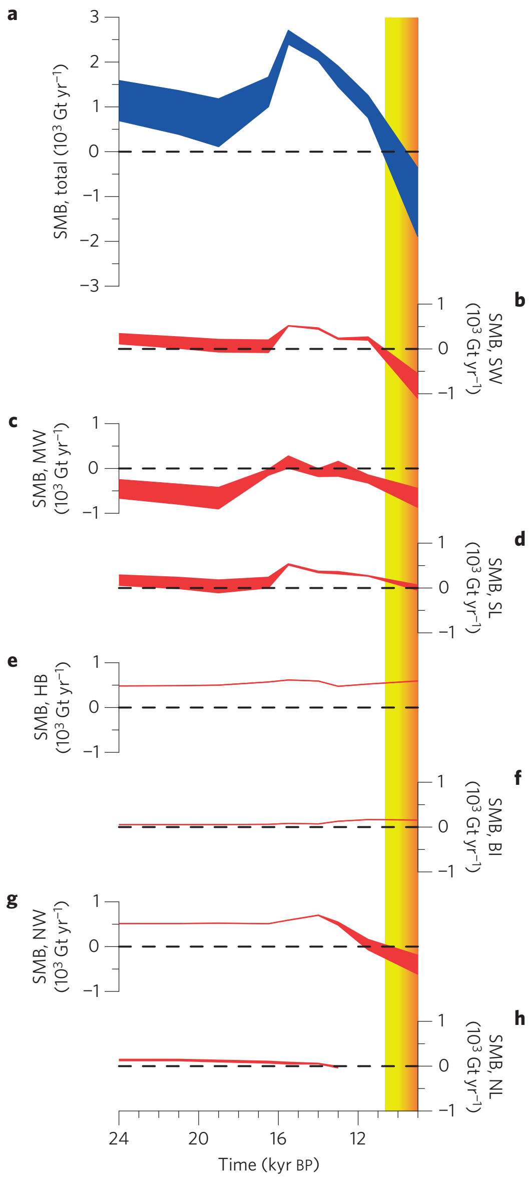

Figure 3 | Regional comparison of deglacial surface mass balance. a, Total LIS surface mass balance (SMB). **b–h**, Regional surface mass balance across each of the seven sectors (locations shown in Fig. 2a): Southwestern (SW; **b**), Midwestern (MW; **c**), St Lawrence (SL; **d**), Hudson Bay (HB; **e**), Baffin Island (BI; **f**), Northwestern (NW; **g**) and Newfoundland (NL; **h**). The range of uncertainty is expressed as the upper (95%) and lower (5%) quantiles from the simulations. The shaded bar indicates the earliest possible timing of the transition to negative total SMB (as shown in Fig. 1).

The spatial distribution of surface mass balance shows that a large part of surface mass loss is confined to low-elevation margins (Fig. 2), particularly the southern low-angle ice lobes[23,24] (Midwestern, Southwestern and Fig. 3), from 24 to 16.5 kyr BP. The greatest accumulation is up-ice of the southern margin, predominantly across the southeastern sector (Midwestern, St Lawrence and Fig. 3) where the maritime influence increases precipitation. At 15.5 and 14 kyr BP, the southern margin ablation area is diminished owing to retreat of the low-angle ice lobes whereas accumulation rates remain similar to earlier intervals, leading to elevated surface mass balance. Starting at 13 kyr BP, the area of ablation begins to expand, particularly across the southern and western margins (Southwestern, Northwestern and Figs 2 and 3). By 9 kyr BP, the extent and magnitude of ablation are sufficient to offset accumulation as total surface mass balance becomes negative (Fig. 1h). Before 13 kyr BP, the northwest sector was probably balanced by dynamic discharge to the Arctic Ocean[28]. The surface mass balance for the Hudson Bay (HB), Baffin Island (BI) and Newfoundland (NL) sectors were largely in equilibrium with climate across the entire suite of simulations, requiring only small dynamic losses to offset accumulation (Figs 2 and 3).

Positive surface mass balance for the entire LIS until after 11.5 kyr BP suggests that dynamical losses were responsible for much of the LIS retreat[6,8,18,21,28] and ~60% of total mass loss up to the Holocene. From 24 to 19 kyr BP, we estimate a dynamical discharge loss of 700–2,500 Gt yr^{-1} (95% confidence) to counterbalance surface mass accumulation and account for associated LIS volume change (Fig. 1i,j), which is in the range of the modern dynamical loss from Antarctic ice sheets (~1,800–2,400 Gt yr^{-1}; ref. 17) over a similar length of marine-terminating margin[23]. The most positive surface mass balance modelled at 15.5 kyr BP implies a dynamic loss of 3,900–4,200 Gt yr^{-1}, which is roughly concurrent with increased LIS iceberg calving during Heinrich event 1 (refs 12,28), although we did not attempt to simulate that event with our climate forcing. The negative surface mass balance at 9 kyr BP in our model may still require dynamical loss of 0–1,500 Gt yr^{-1}. This reduction in dynamical loss coincides with the LIS pullback from the ocean after ~11.5 kyr BP (from ~40% marine-terminating to <15%; ref. 23) and associated evidence for a reduction in ice streaming[28].

Only ~40% of the LIS area loss had occurred by the Holocene[23] (Fig. 1f) despite 40–60 W m^{-2} of rising boreal summer insolation (Fig. 1a) and ~80 ppm increase in atmospheric CO_2 (Fig. 1b). The transition from positive surface mass balance to negative surface mass balance between 11.5 and 9 kyr BP (Fig. 1h), with no abrupt change in surface forcings (Fig. 1d,e), suggests a threshold[9,13,14] was crossed in LIS surface mass balance stability. Following this transition, dynamic influences may have been important in the collapse of ice over Hudson Bay around ~8.2 kyr BP, but this LIS volume reduction was still probably initiated by surface ablation[11,18]. The transition to negative surface mass balance by 9 kyr BP is correlative with an acceleration in LIS retreat (Fig. 1f,g), corroborating the timing of surface mass balance transition in our SEBM results. Much of the LIS retreat occurred in the Holocene at rates two to five times faster than before ~11.5 kyr BP (Fig. 1g)[23], which we simulate to be driven by intensified surface melting.

Our detection of a threshold in LIS surface mass balance has implications for what climate forcing is required to drive a full deglaciation[1–6,15]. Although the latitudinal extent and geometry of the LIS may provide an important precondition for deglaciation possibly driven by dynamic discharge[6,11,18,21,28], our results suggest that full LIS deglaciation would only occur once the combined orbital and greenhouse gas forcing reached peak early Holocene levels, potentially providing a upper limit on this climate threshold[15,16]. Our simulations show that this upper-limiting threshold is a summer surface radiative forcing increase of 16–20 W m^{-2} and summer temperature increase of 6–7 °C over the LIS (Fig. 1d,e) relative to full glacial conditions. Because not all Holocene-like changes in orbital forcing lead to interglaciations[1–4], internal forcing from atmospheric CO_2 may then be the critical differentiator as to whether or not a full deglaciation occurs. However, the mechanisms that caused the rise in atmospheric CO_2 to ~260 ppm during the last deglaciation, or previous deglaciations, are poorly established at present[2,5,7,20]. Nevertheless, our results suggest a two-phased LIS retreat pattern during the last deglaciation, with initial mass loss due to dynamic discharge followed by an unstable surface mass balance-driven retreat during the early Holocene.

Methods

Methods and any associated references are available in the online version of the paper.

Received 15 December 2014; accepted 15 May 2015;
published online 22 June 2015

References

1. Hays, J. D., Imbrie, J. & Shackleton, N. J. Variations in the Earth's orbit: Pacemaker of the ice ages. *Science* **194,** 1121–1132 (1976).
2. Imbrie, J. *et al.* On the structure and origin of major glaciation cycles 2. The 100,000-year cycle. *Paleoceanography* **8,** 699–735 (1993).
3. Raymo, M. E. The timing of major climate terminations. *Paleoceanography* **12,** 577–585 (1997).
4. Carlson, A. E. & Winsor, K. Northern Hemisphere ice-sheet responses to past climate warming. *Nature Geosci.* **5,** 607–613 (2012).
5. Shakun, J. D. *et al.* Global warming preceded by increasing carbon dioxide concentrations during the last deglaciation. *Nature* **484,** 49–55 (2012).
6. Abe-Ouchi, A. *et al.* Insolation-driven 100,000-year glacial cycles and hysteresis of ice-sheet volume. *Nature* **500,** 190–194 (2013).
7. Wolff, E. W., Fischer, H. & Röthlisberger, R. Glacial terminations as southern warmings without northern control. *Nature Geosci.* **2,** 206–209 (2009).
8. Heinemann, M. *et al.* Deglacial ice sheet meltdown: Orbital pacemaking and CO_2 effects. *Clim. Past* **10,** 1567–1579 (2014).
9. Gregory, J. M. & Huybrechts, P. Ice-sheet contributions to future sea-level change. *Phil. Trans. R. Soc. A.* **364,** 1709–1731 (2006).
10. Anslow, F. S. *et al.* Distributed energy balance modeling of South Cascade Glacier, Washington and assessment of model uncertainty. *J. Geophys. Res.* **113,** F02019 (2008).
11. Carlson, A. E. *et al.* Surface-melt driven Laurentide ice sheet retreat during the early Holocene. *Geophys. Res. Lett.* **36,** L24502 (2009).
12. Carlson, A. E. & Clark, P. U. Ice sheet sources of sea level rise and freshwater discharge during the last deglaciation. *Rev. Geophys.* **50,** RG4007 (2012).
13. Lenton, T. M. *et al.* Tipping elements in the Earth's climate system. *Proc. Natl Acad. Sci. USA* **105,** 1786–1793 (2008).
14. Notz, D. The future of ice sheets and sea ice: Between reversible retreat and unstoppable loss. *Proc. Natl Acad. Sci. USA* **106,** 20590–20595 (2009).
15. Calov, R. & Ganopolski, A. Multistability and hysteresis in the climate–cryosphere system under orbital forcing. *Geophys. Res. Lett.* **32,** L21717 (2005).
16. Robinson, A., Calov, R. & Ganopolski, A. Multistability and critical thresholds of the Greenland ice sheet. *Nature Clim. Change* **2,** 429–423 (2012).
17. Rignot, E. *et al.* Acceleration of the contribution of the Greenland and Antarctic ice sheets to sea level rise. *Geophys. Res. Lett.* **38,** L05503 (2011).
18. Gregoire, L. J., Payne, A. J. & Valdes, P. J. Deglacial rapid sea level rises caused by ice-sheet saddle collapses. *Nature* **487,** 219–223 (2012).
19. Laskar, J. *et al.* A long-term numerical solution for the insolation quantities of the Earth. *Astron. Astrophys.* **428,** 261–285 (2004).
20. Parrenin, F. *et al.* Synchronous change of atmospheric CO_2 and Antarctic temperature during the last deglacial warming. *Science* **339,** 1060–1063 (2013).
21. Pollard, D. A simple ice sheet model yields realistic 100 kyr glacial cycles. *Nature* **296,** 334–338 (1982).
22. Weertman, J. Milankovitch solar radiation variations and ice age ice sheet sizes. *Nature* **261,** 17–20 (1976).
23. Dyke, A. S. in *Quaternary Glaciations—Extent and Chronology, Part II* (eds Ehlers, J. & Gibbard, P. L.) 373–424 (Elsevier Science and Technology Books, 2004).
24. Licciardi, J. M. *et al.* Deglaciation of a soft-bedded Laurentide ice sheet. *Quat. Sci. Rev.* **17,** 427–448 (1998).
25. Marshall, S. J., James, T. S. & Clarke, G. K. C. North American ice sheet reconstructions at the last glacial maximum. *Quat. Sci. Rev.* **21,** 175–192 (2002).
26. Pollard, D. *et al.* Comparisons of ice-sheet surface mass budgets from Paleoclimate Modeling Intercomparison Project (PMIP) simulations. *Glob. Planet. Change* **24,** 79–106 (2000).
27. van de Berg, W. J. *et al.* Significant contribution of insolation to Eemian melting of the Greenland ice sheet. *Nature Geosci.* **4,** 679–683 (2011).
28. Stokes, C. R. & Tarasov, L. Ice streaming in the Laurentide ice sheet: A first comparison between data-calibrated numerical model output and geological evidence. *Geophys. Res. Lett.* **37,** L01501 (2010).

Acknowledgements

United States National Science Foundation awards AGS-0753660 (A.E.C.), AGS-0753868 (A.N.L.), and the National Aeronautics and Space Administration supported this research.

Author contributions

A.E.C., A.N.L. and F.S.A. conceived the study; D.J.U., A.N.L., A.E.C. and J.M.L. created deglacial boundary conditions for AOGCM and surface mass balance simulations; A.N.L. conducted GISS ModelE2-R simulations. D.J.U., F.S.A. and A.E.C. implemented the surface energy balance model. D.J.U., A.E.C. and A.N.L. synthesized the results. D.J.U. and A.E.C. wrote the manuscript, with input from all authors.

Additional information

Supplementary information is available in the online version of the paper. Reprints and permissions information is available online at www.nature.com/reprints. Correspondence and requests for materials should be addressed to D.J.U. or A.E.C.

Competing financial interests

The authors declare no competing financial interests.

Methods

Deglacial climate simulations. Deglacial climate was modelled using a fully coupled atmosphere–ocean general circulation model (AOGCM; NASA GISS ModelE2-R; ref. 29). The latest version of ModelE2-R has an atmosphere resolution of 2° latitude by 2.5° longitude, with 40 vertical layers up to 0.1 millibar (mb) height, and an ocean resolution of 1° latitude by 1.25° longitude with 32 depth layers. Separate equilibrium simulations were performed for nine separate time slices (24, 21, 19, 16.5, 15.5, 14, 13, 11.5, and 9 kyr BP). These time steps were chosen because the extent of the Laurentide ice sheet (LIS) is well mapped at each of these time slices[23,30]. We do not attempt to model the meltwater-induced climate fluctuations (for example, the Younger Dryas)[18,31] because of the added uncertainty in this forcing and inconsistency in model response to so-called hosing events[32].

Each time-slice simulation was forced with appropriate insolation[33] and greenhouse gas concentrations[34]. In addition, coastline and basin geometry were adjusted to reflect deglacial changes in sea level from ice-sheet volume changes. LIS topography was assigned using the reconstructions of ref. 24, whereas all other deglacial ice-sheet topographies (Greenland, Scandinavian, and so on) were assigned using the ICE-5G (VM2) global reconstructions[35]. We use the ref. 24 LIS topographies because they more accurately capture the low-elevation lobe geometry of the southern margin[36]. Such a topographic profile, consistent with ice dynamics, is necessary to realistically capture areas of ablation in the simulation of surface mass balance (see Supplementary Figs 1 and 7).

The use of two different reconstructions for the Cordilleran ice sheet (ICE-5G; ref. 35) and the LIS (ref. 24) results in a discontinuity of ice elevation where the ice sheets meet, as the LIS reconstruction does not include any ice-buttressing effects from the Cordilleran, therefore leading to a possible bias towards lower elevations along the western margin in our LIS topography. However, the elevation of the ice along this suture zone is thought to be relatively thin, on the basis of the extent of Laurentide-derived erratics into the Canadian Rockies and flow indicators for the Cordilleran ice sheet[37–40]. Thus, any western margin bias in the ref. 24 reconstruction is likely to be small.

LIS topographies are presented in Supplementary Fig. 1. Note that for time slices 24–19 kyr BP, we do not change LIS topography, as margin fluctuations during this time are small[23,41]. Thus, across these time slices we vary only the insolation forcing (greenhouse gas concentrations are nearly constant according to ice-core records[34]).

Each time-slice simulation was run to equilibrium. After 1,500 years of integration, long-term drift in surface air temperature, sea surface temperature, and deep ocean temperature were all less than 0.03 °C per century. Even though we apply this equilibrium approach across a transient deglaciation, our simulations compare favourably with the reconstruction of Northern Hemisphere temperature[5] (Fig. 1c).

Because we force our surface mass balance model (see below) directly with AOGCM output, it is necessary to evaluate the general bias in the climate simulations. For the historical period, where direct climate measurements are available, ModelE2-R performs in the 'middle of the pack' amongst all Coupled Model Intercomparison Project Phase 5 (CMIP5) models for temperature and precipitation[42]. Perhaps more relevant for an examination of the deglaciation is its performance on snow ice albedo feedbacks. Here ModelE2-R outperforms nearly all of the CMIP5 models[43]. For general climate sensitivity, ModelE2-R also performs fairly well, within 1 s.d. of the median value of observed climate sensitivity, calculated over the past 50 years[44].

For North America specifically, ref. 45 provides a overview of the performance of all CMIP5 models. The biases in temperature and precipitation for ModelE2-R show a winter −0.33 °C and summer −0.64 °C overall North American temperature bias, with northeastern Canada having a positive 1 °C winter and 0.79 °C summer bias. The precipitation bias over this area is 15% in winter and 11% in summer. These values place ModelE2-R in the mid-range for biases. It would be an interesting experiment to apply these biases and see how the LIS surface mass balance results are influenced. However, it is not clear that during the deglacial period that the biases would be the same; the jet stream is displaced southwards during the deglaciation and specific humidity is overall lower. Positive temperature and precipitation biases would probably counteract one another (slightly cancel) in changing equilibrium line altitude (ELA).

Assessing model bias across the deglaciation is more difficult as we are limited to comparisons with reconstructions and proxy measurements. Nevertheless, we believe that our ModelE2-R results provide a fairly accurate assessment of the deglacial temperature and hydrologic change, as indicated by our comparisons with the ref. 5 Northern Hemisphere temperature reconstruction (Fig. 1c). The inclusion of water isotope tracers in ModelE2-R allows direct comparison with proxy measurements of δ^{18}O in precipitation from ice cores and speleothems. We specifically select only those δ^{18}O records that span the entire deglaciation (see Supplementary Table 1).

Model tracers match the general patterns in δ^{18}O of precipitation (δ^{18}Oa) from proxy records (refs 46–58, Supplementary Fig. 2). The notable exception is the 9 kyr BP simulation, showing a lack of significant correlation between model and data δ^{18}O anomalies. We believe that there may be three reasons explaining this lack of correlation. The first issue is the low signal-to-noise ratio for Holocene δ^{18}Oa anomalies. For most records, the difference in δ^{18}Oa between 9 kyr BP and the pre-industrial is fairly small, so a slight bias in the model or error in proxy measurement could switch the direction of change (positive or negative), providing a negative impact on model–data correlation.

Second, three of the records in our δ^{18}Oa database come from Greenland ice cores. Each of these data records have a slight positive anomaly in δ^{18}Oa at 9 kyr BP, whereas our simulations show a slight negative anomaly. However, in our ice-sheet boundary conditions in the AOGCM, we use ICE-5G (refs 35,59) for all non-LIS ice sheets. Recent modelling in ref. 60 has significantly revised the Greenland ice-sheet topography in the early Holocene, which could explain some of the offset between model and data at these sites.

Third, a number of our other observational sites that do not correlate well with the model at 9 kyr BP actually occur near shifts in the positive/negative δ^{18}Oa anomaly front. A shift in this front by less than a few hundred kilometres in the model may have provided a better correlation. Many of these sites have complex surrounding topographies, which may drive such local edge effects not captured in our model. The smaller δ^{18}Oa anomalies at 9 kyr BP again make it difficult to capture the signal as compared with the earlier time periods with larger global climate change.

Surface energy balance model. The equilibrium output from each time-slice simulation was used to force the surface energy balance model (SEBM) of ref. 10, using the downscaling method of ref. 11 onto 10 km × 10 km grids of LIS topography for each time slice (Supplementary Fig. 1)[24]. The use of this SEBM is advantageous over the standard positive degree-day (PDD) methods[10,11] by incorporating more of the climate-driven surface processes that complicate surface mass balance, particularly those related to the resolution of refreezing rates at the surface[27,61,62]. The SEBM can be adjusted with variables from different ice-surface conditions, such as snow/ice roughness and temporal changes of albedo through a melt season. We assign these variables to match the range of observations from the Greenland and Antarctic ice sheets[11,63–66]. We then conducted 1,000 Monte Carlo simulations for each time slice to assess the range of parametric uncertainty in surface mass balance due to variability in the SEBM sensitivity parameters. The uncertainty range in SEBM results is expressed as the upper and lower 95% quantiles of the distribution of surface mass balance results from those experiments (Fig. 1h). This range of surface mass balance estimates is used to infer the range of possible dynamical discharge amounts (also upper and lower 95% quantiles) by subtracting the surface mass balance estimates from the rate of change in volume across the LIS recontructions[24] (Fig. 1j).

The SEBM results are dependent on model resolution, as lower-resolution reconstructions of the ice-sheet topography can lead to large jumps in the area extent above or below the equilibrium line[67]. A previous study using lower-resolution AOGCM output to force an earlier version of our surface mass balance model found that the ice-sheet resolution (from 100 km down to 10 km) did not have an effect on total surface mass balance at 9 kyr BP (ref. 11). However, given updates to the surface mass balance model to better simulate a realistic equilibrium line altitude, as well as a diverse array of ice-sheet geometries across the deglaciation, we conducted a series of resolution tests at each time slice using a fixed set of the model's sensitivity parameters and found that the SEBM results did not stabilize until resolutions of 10 km (Supplementary Fig. 3), allowing us to select the optimal resolution to be 10 km. Owing to the high computational expense at this resolution, we also ran simulations at 50 km resolution as an initial test of the SEBM and Monte Carlo approach. When we include our model uncertainty (expressed as the range of results from our Monte Carlo simulations), the results at 10 and 50 km resolution are nearly consistent across all time slices (Supplementary Fig. 4). This match in the results from different resolutions suggests that although for a given set of SEBM parameters there may be large differences in the resulting surface mass balance until resolutions of 10 km and higher (Supplementary Fig. 3), the parametric uncertainty included in our Monte Carlo approach spans the effects of resolution uncertainty.

The SEBM has a base albedo that is exposed when all snow melts on the surface. This base albedo approaches 0.85 and 0.45 above and below the equilibrium line, respectively. We prescribe an initial ELA at 45° N using a linear trend in ELA from 2,000 m at the last glacial maximum to 3,000 m at 11.5 kyr BP, as suggested by cirque elevations from the American Rockies[68–70]. These values are for initialization as the effective snowline evolves in the SEBM with changes in conditions over the melt season. Given the large latitudinal extent of the LIS, we also assign a latitudinal dependence of −150 m per degree latitude in the initial ELA to match similar trends across Cordilleran glaciers and the Greenland ice sheet[71,72].

We tested the impact of GISS ModelE-R bias in our SEBM forcings by applying perturbations of ±1 °C in surface air temperatures and ±15% for precipitation, for a median set of SEBM sensitivity parameters. This uniform perturbation does impact the overall magnitude of the surface mass balance, but the general deglacial trend is maintained (Supplementary Fig. 5). Particularly, surface mass balance does not reach values that are more negative than the last glacial maximum (LGM) conditions (24–19 kyr BP) until after 11.5 kyr BP in each of these perturbed runs. To the extent that the LGM ice sheet was nearly stable at the LGM, such negative anomalies from the LGM state provide a consistent transition in the LIS surface mass balance, regardless of SEBM forcing bias from GISS ModelE-R. However, we show these results only to demonstrate that even extreme AOGCM bias would not affect our final conclusions. We also choose not to include such forcing bias in our final assessment of surface mass balance because such perturbations are slightly arbitrary, any model bias is unlikely to have been spatially and temporally uniform across the AOGCM as applied in these sensitivity analyses, and such temperature/precipitation forcing perturbations are not in equilibrium with the LIS topographic boundary conditions as in our standard simulations.

We calculate regional surface mass balance (SMB) averages to determine the sectors of the LIS that dominate surface mass loss/gain. These regions were assigned using topographic divides in the LIS reconstruction to separate ice drainage areas, as shown in Supplementary Fig. 1.

Positive degree-day (PDD) calculations. To compare our SEBM with the tradition PDD ablation methods used in previous studies of LIS mass balance, we apply a modified PDD scheme that was developed for the Greenland ice sheet[25,73,74], using daily AOGCM output (temperature, precipitation, and evaporation) lapsed to a LIS topography at 50 km resolution. The PDD surface mass balance (SMB) at each grid point (i,j) is calculated as:

$$\mathrm{SMB}_{i,j} = P_{i,j} - E_{i,j} - \mathrm{PDDmelt}_{i,j}(1 - r_f)$$

and

$$\mathrm{PDDmelt}_{i,j} = \begin{cases} 0, \quad \mathrm{SAT} \leq 273.15\,\mathrm{K} \\ f_{\mathrm{ice}}(\mathrm{SAT}_{i,j} - 273.15) + f_{\mathrm{snow}}(\mathrm{SAT}_{i,j} - 273.15), \\ \mathrm{SAT} > 273.15 \end{cases}$$

$$f_{\mathrm{ice}} = \begin{cases} 7\text{–}9\,\mathrm{mm\,yr^{-1}}, \mathrm{SWE} < 1\,\mathrm{mm} \\ 0, \ \mathrm{SWE} \geq 1\,\mathrm{mm} \end{cases}$$

$$f_{\mathrm{snow}} = \begin{cases} 2\text{–}4\,\mathrm{mm\,yr^{-1}}, \mathrm{SWE} \geq 1\,\mathrm{mm} \\ 0, \ \mathrm{SWE} < 1\,\mathrm{mm} \end{cases}$$

where P is precipitation, E is evaporation, f_{ice} is the degree-day factor for bare ice [applied only over areas where snow depth (that is, snow water equivalent, SWE) is less than 1 mm], f_{snow} is the degree-day factor for areas of snow cover (SWE $\geq$ 1 mm), r_f is fraction of surface melt that refreezes to the ice, and SAT is surface air temperature. Following ref. 25, we apply a range of values for f_{ice} (7–9 mm yr^{-1} K^{-1}), f_{snow} (2–4 mm yr^{-1} K^{-1}) and r_f (0.3–0.8). Total annual surface mass balance is calculated as the sum of each daily calculated surface mass balance, converted to Gt yr^{-1} by multiplying by the area of each grid cell and the density of water. The range of PDD surface mass balance (Fig. 1h) uses the upper and lower bound in the PDD results due to the range in the PDD constants.

Although the range of PDD factors listed above encompasses those used in previous PDD analyses of LIS surface mass balance[6,8,18,25], observations suggest that higher values may be possible[74]. If we instead use maximum observed PDD factors of 13.8 mm yr^{-1} (ice) and 5.7 mm yr^{-1} (snow) from ref. 74, the PDD scheme results in a temporal evolution of surface mass balance that is more similar to our SEBM solution, with slightly negative values at 9 kyr BP (Supplementary Fig. 6). However, this maximum-melt PDD calculation does not capture the more positive values between 16.5–13 kyr BP. Although we do not have a constraint on PDD for the LIS, we favour the range of PDD factors used in previous analyses, as these maximum values are probably unrealistic for much of an ice sheet the size of the LIS (ref. 74). However, these maximum-melt PDD results provide an indication that higher degree-day factors than those used in previous analyses may be necessary to approach the energy balance solution.

Surface energy balance of ICE-5G. To determine the impact of the reconstructed LIS topography on modelled surface mass balance, we conducted an additional set of paired AOGCM–SEBM simulations at 21 and 14 kyr BP using the geophysically based reconstruction of the LIS, ICE-5G (ref. 35), instead of the ref. 24 flow-line reconstruction. The topography in the ICE-5G reconstruction is substantially higher in elevation than in ref. 24, particularly the Keewatin Dome in western Canada[75]. In addition, ICE-5G has abrupt transitions in topography across the LIS from high to low regions, unlike the smoother transition in the ref. 24 reconstruction. Owing to computational constraints, these topographic sensitivity simulations were conducted at a resolution of 50 km.

In the 21 kyr BP simulation, the Monte Carlo-based range of total surface mass balance over the ICE-5G LIS is significantly higher than with the ref. 24 reconstruction (2,700–3,100 Gt yr^{-1} and 250–1,300 Gt yr^{-1}, respectively). This difference is particularly driven by the lack of ablation along most of the southern margin in the ICE-5G simulation (Supplementary Fig. 7). The ref. 24 ice sheet has greater accumulation across the western interior, where its topography is greatly reduced relative to ICE-5G. However, the additional surface mass losses along the southern margin in the ref. 24 simulation compensate for this accumulation in the total ice-sheet surface mass balance.

At 14 kyr BP, the ICE-5G simulation results in a surface mass balance that overlaps with the standard (ref. 24) simulation (1,300–2,200 Gt yr^{-1} and 700–1,800 Gt yr^{-1}, respectively), but the lack of ablation along the southern margin in the ICE-5G simulation again leads to the slight increase in overall surface mass balance (Supplementary Fig. 7). In addition, the 14 kyr BP ICE-5G simulation has a region of ablation north of Lake Superior away from the margin. Were it not for this unlikely ablation zone, the ICE-5G surface mass balance would again be substantially higher than our standard (ref. 24) 14 kyr BP simulation.

As surface melt across the fairly narrow low-elevation ablation zones provides the dominant control on overall surface mass balance losses (see text), proper ice-margin resolution is necessary to adequately simulate LIS surface mass balance and its evolution throughout deglaciation. The southern margin resolution in ICE-5G is much too coarse to capture this necessary spatial variability in surface mass balance.

Code availability. The code used in the surface energy balance model is available in the Supplementary Information.

References

29. Schmidt, G. A. *et al.* Configuration and assessment of the GISS ModelE2 contributions to the CMIP5 archive. *J. Adv. Model. Earth Syst.* **6,** 141–184 (2014).
30. Dyke, A. S. & Prest, V. K. Late Wisconsinan and Holocene history of the Laurentide ice sheet. *Geogr. Phys. Quat.* **41,** 237–263 (1987).
31. Liu, Z. *et al.* Transient simulation of the last deglaciation with a new mechanism for Bølling–Allerød warming. *Science* **325,** 310–314 (2009).
32. Kageyama, M. *et al.* Modelling glacial climatic millennial-scale variability related to changes in the Atlantic meridional overturning circulations: A review. *Quat. Sci. Rev.* **29,** 2931–2956 (2010).
33. Berger, A. & Loutre, M. F. Isolation values for the climate of the last 10 million years. *Quat. Sci. Rev.* **10,** 297–317 (1991).
34. Joos, F. & Spahni, R. Rates of change in natural and anthropogenic radiative forcing over the past 20,000 years. *Proc. Natl Acad. Sci. USA* **105,** 1425–1430 (2008).
35. Peltier, W. R. Global glacial isostasy and the surface of the ice-age earth: The ICE-5G (VM2) model and GRACE. *Annu. Rev. Earth Planet. Sci.* **32,** 111–149 (2004).
36. Clark, P. U. Surface form of the southern Laurentide ice sheet and its implications to ice-sheet dynamics. *GSA Bull.* **104,** 595–695 (1992).
37. Bobrowsky, P. & Rutter, N. W. The Quaternary geologic history of the Canadian Rocky Mountains. *Géogr. Phys. Quat.* **46,** 5–50 (1992).
38. Catto, N. *et al.* Laurentide, Cordilleran, and montane glaciation in the Western Peace River – Grande Prairie Region, Alberta and British Columbia, Canada. *Quat. Int.* **32,** 21–32 (1996).
39. Hartman, G. M. D. & Clague, J. J. Quaternary stratigraphy and glacial history of the Peace River valley, northeast British Columbia. *Canad. J. Earth Sci.* **45,** 549–564 (2008).
40. Margold, M. *et al.* Retreat pattern of the Cordilleran ice sheet in central British Columbia at the end of the last glaciation reconstructed from glacial meltwater landforms. *Boreas* **42,** 830–847 (2013).
41. Ullman, D. J. *et al.* Southern Laurentide ice-sheet retreat synchronous with rising boreal summer insolation. *Geology* **43,** 23–26 (2015).
42. Knutti, R., Masson, D. & Gettelman, A. Climate model geneaology: Generation CMIP5 and how we got there. *Geophys. Res. Lett.* **40,** 1194–1199 (2013).
43. Qu, X. & Hall, A. On the persistent spread in snow-albedo feedback. *Clim. Dynam.* **42,** 69–81 (2013).
44. Masters, T. Observational estimate of climate sensitivity from changes in the rate of ocean heat uptake and comparison to CMIP5 models. *Clim. Dynam.* **42,** 2173–2181 (2014).
45. Sheffield, J. *et al.* North American climate in CMIP5 experiments, Part I: Evaluation of historical simulations of continental and regional climatology. *J. Clim.* **26,** 9209–9245 (2013).
46. Dansgaard, W. *et al.* Evidence for general instability of past climate from a 250-kyr ice-core record. *Nature* **364,** 218–220 (1993).
47. Grootes, P. M. *et al.* Comparison of oxygen isotope records from the GISP2 and GRIP Greenland ice cores. *Nature* **366,** 552–554 (1993).
48. Thompson, L. G. *et al.* A 25,000-year tropical climate history from Bolivian ice cores. *Science* **282,** 1858–1864 (1998).
49. Wang, Y. J. *et al.* A high-resolution absolute-dated late Pleistocene monsoon record from Hulu Cave, China. *Science* **294,** 2345–2348 (2001).

50. Bar-Matthews, M. *et al.* Sea-land oxygen isotopic relationships from planktonic foraminifera and speleothems in the Eastern Mediterranean region and their implication for paleorainfall during interglacial intervals. *Geochim. Cosmochim. Acta* **67,** 3181–3199 (2003).
51. Holmgren, K. *et al.* Persistent millennial-scale climatic variability over the past 25,000 years in Southern Africa. *Quat. Sci. Rev.* **22,** 2311–2326 (2003).
52. Cruz, F. W. *et al.* Insolation-driven changes in atmospheric circulation over the past 116,000 years in subtropical Brazil. *Nature* **483,** 63–66 (2005).
53. Dykoski, C. A. *et al.* A high-resolution, absolute-dated Holocene and deglacial Asian monsoon record from Dongge Cave, China. *Earth Planet. Sci. Lett.* **233,** 71–86 (2005).
54. Williams, P. W. *et al.* Late Pleistocene to Holocene composite speleothem ^{18}O and ^{13}C chronologies from South Island, New Zealand—did a global Younger Dryas really exist? *Earth Planet. Sci. Lett.* **230,** 301–317 (2005).
55. Partin, J. *et al.* Millennial-scale trends in west Pacific warm pool hydrology since the Last Glacial Maximum. *Nature* **449,** 452–455 (2007).
56. Wang, X. *et al.* Millennial-scale precipitation changes in southern Brazil over the past 90,000 years. *Geophys. Res. Lett.* **34,** L23701 (2007).
57. Svensson, A. *et al.* A 60 000 year Greenland stratigraphic ice core chronology. *Clim. Past.* **4,** 47–57 (2008).
58. Cheng, H. *et al.* The climatic cyclicity in semiarid-arid central Asia over the past 500,000 years. *Geophys. Res. Lett.* **39,** L01705 (2012).
59. Tarasov, L. & Peltier, W. R. Greenland glacial history and local geodynamic consequences. *Geophys. J. Int.* **150,** 198–229 (2002).
60. LaCavalier, B. S. *et al.* A model of Greenland ice sheet deglaciation constrained by observations of relative sea level and ice extent. *Quat. Sci. Rev.* **21,** 175–192 (2014).
61. van de Wal, R. S. W. Mass-balance modeling of the Greenland ice-sheet: A comparison of an energy balance and a degree-day model. *Ann. Glaciol.* **23,** 36–45 (1996).
62. Bougamont, M. *et al.* Impact of model physics on estimating the surface mass balance of the Greenland ice sheet. *Geophys. Res. Lett.* **34,** L17501 (2007).
63. Grainger, M. E. & Lister, H. Wind speed, stability and eddy viscosity over melting ice surfaces. *J. Glaciol.* **6,** 101–127 (1966).
64. Duynkerke, P. G. & van den Broeke, M. R. Surface energy balance and katabatic flow over glacier and tundra during GIMEX-91. *Glob. Planet. Change* **9,** 17–28 (1994).
65. Greuell, W. & Konzelmann, T. Numerical modeling of the energy balance and the englacial temperature of the Greenland ice sheet. Calculations for the ETH-Camp location (West Greenland, 1155 m a.s.l.). *Glob. Planet. Change* **9,** 91–114 (1994).
66. Smeets, C. J. P. P. & van den Broeke, M. R. Temporal and spatial variations of the aerodynamic roughness length in the ablation zone of the Greenland ice sheet. *Bound.-Lay. Meteorol.* **128,** 315–338 (2008).
67. van den Berg, J., van de Wal, R. S. W. & Oerlemans, J. Effects of spatial discretization in ice-sheet modeling using the shallow-ice approximation. *J. Glaciol.* **52,** 89–98 (2006).
68. Porter, S. C. *et al.* in *Late Quaternary Environments of the United States* Vol. 1 (eds Wright, H. E. Jr & Porter, S. C.) 71–111 (University of Minnesota Press, 1983).
69. Davis, P. T. Holocene glacier fluctuations in the American Cordillera. *Quat. Sci. Rev.* **7,** 129–157 (1988).
70. Pierce, K. L. Pleistocene glaciations of the Rocky mountains. *Dev. Quat. Sci.* **1,** 63–76 (2003).
71. Broecker, W. S. & Denton, G. H. The role of ocean-atmosphere reorganizations in glacial cycles. *Quat. Sci. Rev.* **9,** 305–341 (1990).
72. Zwally, H. J. & Giovinetto, M. B. Balance mass flux and ice velocity across the equilibrium line in drainage systems of Greenland. *J. Geophys. Res.* **106,** 33717–33728 (2001).
73. Reeh, N. Parameterization of melt rate and surface temperature on the Greenland ice sheet. *Polarforschung* **53,** 113–128 (1991).
74. Braithwaite, R. J. Positive degree-day factors for ablation on the Greenland ice sheet studied by energy-balance modelling. *J. Glaciol.* **41,** 153–160 (1995).
75. Ullman, D. J. *et al.* Assessing the impact of Laurentide ice-sheet topography on glacial climate. *Clim. Past* **10,** 487–507 (2014).